

O/N Co-Doped, Layered Porous Carbon with Mesoporosity up to 99 % for Ultrahigh-Rate Capability Supercapacitors

Bei Liu,^[a] Jikai Wen,^[a] Hongbiao Chen,^{*[a]} Mei Yang,^[a] Yijang Liu,^[a] and Huaming Li^{*[a, b]}

Ultrahigh-rate capability supercapacitors that can tolerate charging/discharging at ultrahigh current density are particularly attractive for high-power applications. At present, mesopore-engineering and heteroatom-doping have been proven to be the effective ways for concurrently enhancing energy density and rate capability. Herein, we report the fabrication of O/N-co-doped mesoporous carbons with ultrahigh mesoporosity and well-defined mesopores by one-step Na_2CO_3 -activation of covalent triazine-based frameworks that derive from 2,4,6-tris(4-cyanophenoxy)-1,3,5-triazine monomer (CTFO) at 800–1000 °C.

The as-obtained O/N-co-doped carbon (CTFC-900) with up to 99% mesoporosity possesses a layered structure together with a high specific surface area ($2425 \text{ m}^2 \text{ g}^{-1}$) and a high N/O content (6.98 at% N and 10.32 at% O). Owing to these merits, the supercapacitor based on CTFC-900 electrode exhibited a high specific capacitance of 287 F g^{-1} at 1.0 A g^{-1} and an ultrahigh rate capability of 66.1% at $1\text{--}1000 \text{ A g}^{-1}$ in alkaline electrolyte. Moreover, the CTFC-900-based supercapacitor in neutral electrolyte achieved both high energy density (32.2 Wh kg^{-1}) and high power density (187 kW kg^{-1}).

1. Introduction

Supercapacitors by virtue of high power density, long lifecycle, and environmental friendliness have always been the research hotspots in the field of electrochemical energy storage systems.^[1–3] Although supercapacitors have been developed for several decades, the energy density is still much lower as compared to batteries and fuel cells. For instance, most of the carbon-based supercapacitors have an energy density of less than 10 Wh kg^{-1} , which remains a big challenge for practical applications.^[4–6] As a result, supercapacitors are usually used in conjunction with other high energy density storage devices, i.e., lithium-ion batteries.^[7,8] Besides, in order to meet the specific requirements of high-power application, the rate capability of supercapacitors should be further improved. Therefore, research effort has been focused on the high energy density and high-rate capability supercapacitors.^[9–12] In recent years, two main strategies including optimization design of electrode materials and hybridization of supercapacitor configurations (namely asymmetric supercapacitor) have been adopted to realize these goals.^[9–14] Among them, electrode material design and optimization have great potential to simultaneously achieve high energy density and high-rate capability.^[9–11,13] Currently, the commonly used supercapacitor

electrode materials are non-faradaic materials (i.e., porous carbon materials^[4–6,9]) and faradaic materials (i.e., transition metal oxides, hydroxides and nitrides,^[12,15,16–18] and conducting polymers^[19–21]), of which porous carbon materials have been extensively investigated due to their high stability, high conductivity, low cost, and tunable specific surface area (SSA) and pore structure.^[4–6,9,13]

Considering that the energy storage and the rate capability of carbon-based supercapacitors are directly related to the SSA along with the pore structure of carbon materials, pore engineering seems to be an efficient way of concurrently enhancing energy density and rate capability.^[9,22] Although fine-tuned microporous carbons can achieve the maximum capacitance with a pore size of 0.7 nm in aqueous media and 0.8 nm in organic media,^[23,24] such micropores will not be accessible to electrolyte ions at high current densities and that leads to a poor-rate performance.^[25,26] In this scenario, carbon materials with well-balanced micro- and mesoporosity have been proposed for the improvement of rate capability.^[27–30] Despite efforts to address this problem, there is still a long way to go in the pursuit of ultrahigh-rate capability. At present, it is widely accepted that pore-size regulation and heteroatom-doping of mesoporous carbon materials play an increasingly important role in the improvement of both rate capability and energy density.^[9] This is due to the fact that such mesoporous carbons with proper pore size are expected not only to have high SSA for high energy storage, but also to provide pore channels for fast electrolyte-ion transport.^[31] Similarly, heteroatom-doping in mesoporous carbons can not only produce pseudo-active functionalities for increasing capacitance, but also improve the wettability for maximum accessibility of electrolyte ions and subsequently reduce the internal resistance.^[22,31] Up to now, although ordered mesoporous carbons that fabricated by either nanocasting (also known as hard-templating) or soft-templating synthesis strategies have been widely investigated, the relatively low SSA (i.e., typically

[a] Dr. B. Liu, J. Wen, Prof. H. Chen, Dr. M. Yang, Dr. Y. Liu, Prof. H. Li
College of Chemistry,
Xiangtan University,
Xiangtan 411105, Hunan Province, P. R. China
E-mail: chhb606@163.com

[b] Prof. H. Li
Key Laboratory of Polymeric Materials & Application Technology of Hunan Province, and Key Laboratory of Advanced Functional Polymeric Materials of College of Hunan Province, Xiangtan University, Xiangtan 411105, Hunan Province, P. R. China
E-mail: lihuaming@xtu.edu.cn

 Supporting information for this article is available on the WWW under
<https://doi.org/10.1002/batt.202000037>

below $1500 \text{ m}^2 \text{ g}^{-1}$) cannot deliver high energy densities.^[32,33] On the contrary, heteroatom-doped, disordered mesoporous carbons with high SSA together with narrow pore-size distribution can fulfill the requirements of high energy density and high-rate performance.^[31] Especially, mesoporous carbons with pore-size in the range of 2–5 nm are more favorable for the simultaneous enhancement of rate capability and energy density.^[34–38] This is due to the fact that pore sizes below 2 nm cannot ensure fast ionic transport, whereas pore sizes above 5 nm will decrease the SSA and resulting in low energy storage.^[39,40]

Current strategies for the fabrication of heteroatom-doped, disordered mesoporous carbons include templating strategies using both hard- and soft-templates, as well as activation strategies involving the use of chemical activation agents.^[9,31,41] By comparison, chemical activation method is easier operation and more time-saving, since both hard- and soft-template syntheses and hard-template removals are often time-consuming. But on the other hand, mesoporous carbons fabricated by using of highly corrosive activation agents (i.e., KOH) would inevitably contain a certain amount of micropores, let alone control mesopore-size distribution.^[9,42] For the purpose of synthesizing mesoporous carbons that have high SSA along with narrow pore-size distribution, carbon precursors that combine high SSA with well-defined, small-sized pores should be selected. If those precursors can be activated in such a manner that only causes the pores to become enlarged, but without producing additional micropores through the selection of activation agents (i.e., weakly corrosive Na_2CO_3), mesoporous carbons with high percentage of mesopore volume together with well-defined mesopores can be fabricated in this way. Recently, covalent triazine-based frameworks (CTFs) have emerged as an attractive precursor for the fabrication of such mesoporous carbons.^[43–45] Owing to the covalent attachment of rigid aromatic building blocks, these N-enriched CTFs can meet the requirements of high SSA along with narrowly distributed micropores.^[43,44] Besides, CTFs can be facilely synthesized by ZnCl_2 triggered cyclotrimerization of carbonitrile monomers and their properties such as porosity, SSA, and N- or other heteroatom-contents can also be finely tuned by monomer design.^[45,46]

Herein, we report the fabrication of O/N-co-doped mesoporous carbon by one-step Na_2CO_3 activation of CTF precursor that derived from 2,4,6-tris(4-cyanophenoxy)-1,3,5-triazine monomer (namely CTFO). The CTFO precursor synthesized by ZnCl_2 -mediated ionothermal trimerization possessed a relatively high SSA of $851 \text{ m}^2 \text{ g}^{-1}$ along with a pore-size distribution of 0.5–3 nm. After one-step Na_2CO_3 -activation at 900°C , the obtained O/N-co-doped mesoporous carbon (namely CTFC-900) had a layered structure as well as a high SSA ($2425 \text{ m}^2 \text{ g}^{-1}$) and a high total pore volume ($1.46 \text{ cm}^3 \text{ g}^{-1}$). The mesoporosity of CTFC-900 was up to 99% with mesopore size in the range of 2–5 nm. Besides, the high N/O contents (6.98 at% N and 10.32 at% O) of CTFC-900 were endowed with not only enhanced wettability but also additional faradaic capacitance. Owing to these merits, the CTFC-900-based supercapacitor exhibited a high specific capacitance of 287 F g^{-1} at 1.0 A g^{-1}

and an ultrahigh rate capability of 66.1% at $1\text{--}1000 \text{ A g}^{-1}$ in alkaline electrolyte. In addition, the CTFC-900-derived supercapacitor in neutral electrolyte achieved both high energy density (32.2 Wh kg^{-1}) and high power density (187.3 kW kg^{-1}).

2. Results and Discussion

2.1. Fabrication and Characterization of CTFC-x

In the present study, the CTFO precursor was synthesized by ZnCl_2 -mediated ionothermal polytrimerization. Elemental analysis result indicated that the N content in CTFO was slightly lower than that of calculated value (Table S1), indicating the occurrence of partial carbonization during the high-temperature polytrimerization. The SSA and total pore volume (V_{total}) were determined to be $851 \text{ m}^2 \text{ g}^{-1}$ and $0.49 \text{ cm}^3 \text{ g}^{-1}$, respectively, for the CTFO (Figure 1a), of which around 56% of the V_{total} value was contributed by the micropores (Table S2). The pore-size distribution of CTFO was in the range of 0.4–3.0 nm (Figure 1b). As can be seen, the high SSA along with narrowly distributed, small-sized pores of CTFO makes it an ideal precursor for the fabrication of mesoporous carbons. The CTFO precursor was therefore directly Na_2CO_3 -activated at $900\text{--}1000^\circ\text{C}$, yielding O/N-co-doped mesoporous carbons that were named as CTFC-800, CTFC-900, and CTFC-1000, respectively. The optimal mass ratio of CTFO/ Na_2CO_3 was determined to be 1/1 (Figure S3). By comparison with CTFO/ Na_2CO_3 mass ratio, the activation temperature exerts a greater impact on the textural properties of these mesoporous carbons. When the activation temperature rose, the SSA and V_{total} values of the CTFC carbons increased correspondingly but exhibited a maximum SSA and V_{total} values at 900°C . The SSA and V_{total} values were determined to be $1968 \text{ m}^2 \text{ g}^{-1}$ and $1.20 \text{ cm}^3 \text{ g}^{-1}$, $2425 \text{ m}^2 \text{ g}^{-1}$ and $1.46 \text{ cm}^3 \text{ g}^{-1}$, and $2217 \text{ m}^2 \text{ g}^{-1}$ and $1.37 \text{ cm}^3 \text{ g}^{-1}$, respectively, for the CTFC-800, CTFC-900, and CTFC-1000 carbons (Figure 1a, Table S2). Notably, such CTFC carbons possessed extremely high mesoporosity (defined as the ratio of mesopore volume (V_{meso}) to V_{total} , i.e., $V_{\text{meso}}/V_{\text{total}}$). For example, the mesoporosity of the CTFC-900 and CTFC-1000 carbons can be as high as 99% (Figure 1c). These results demonstrate that the weakly corrosive Na_2CO_3 can only enlarge the pore size, but cannot create additional micropores. With increasing temperature, the pore-size gradually increased from 0.4–3.0 nm for the CTFO precursor to 0.8–4.0 nm for the CTFC-800, 2.0–5.0 nm for the CTFC-900, and 2.0–5.5 nm for the CTFC-1000 carbons (Figure 1b). These results indicate that the Na_2CO_3 -activation can enlarge the pore size by up to about 2 nm but depends on the activation temperature. At a low activation temperature of 800°C , the activation reactions could only occur between Na_2CO_3 and carbon alongside surface-attached O/N-containing functional groups (Figure S5),^[47,48] as demonstrated by the TGA analysis (Figure S4). However, such activation reactions are less effective and result in incomplete transformation of micropores. At high activation temperatures ($>800^\circ\text{C}$), the activation reactions involving Na_2CO_3 and CO_2 both occurred (Figure S5), leading to a complete transformation of micropores. In fact,

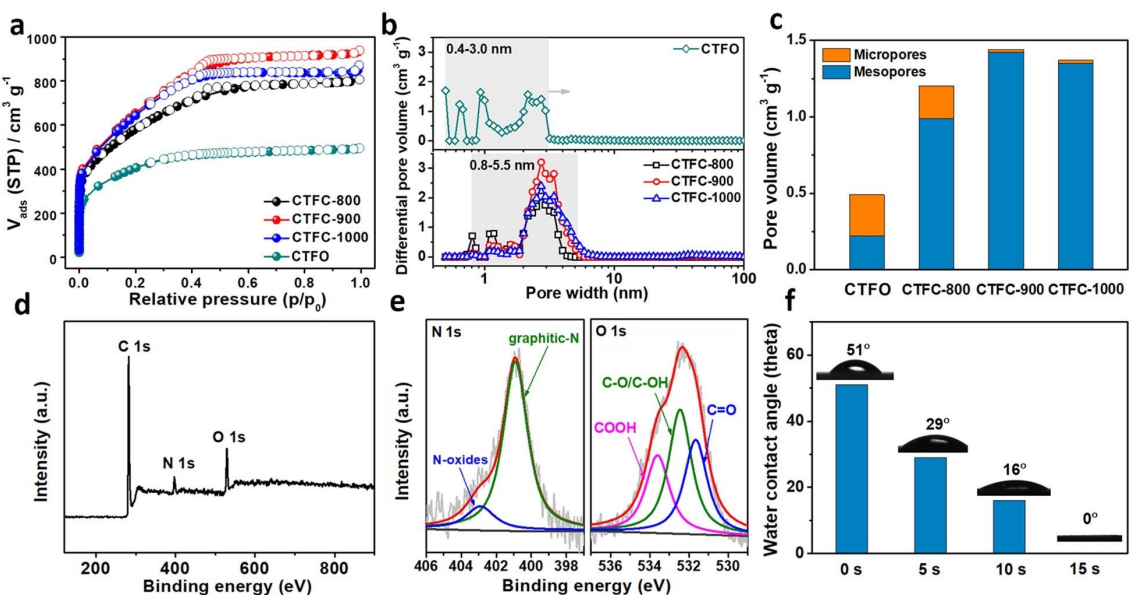


Figure 1. a) N_2 adsorption/desorption isotherms, b) pore size distributions, and c) pore volumes for CTFO and CTFC carbons. d) XPS survey spectrum, e) deconvoluted N 1s and O 1s peaks, and f) dynamic contact angle tests of CTFC-900.

such smaller mesopores can be further transformed into bigger mesopores at sufficiently high activation temperature, i.e., 1000 °C, while the SSA value decreases in turn since larger mesopores are usually in contradiction with SSA value. Considering that the activation agent Na_2CO_3 can exist either in the pores or on the surfaces of the CTFO precursor, such activation reactions should, of course, occur within the pores or on the surfaces, in which activation reactions occurred within the pores are less corrosive and can only enlarge the pores instead of creating micropores. In contrast to Na_2CO_3 -activation, KOH-activation would inevitably lead to the formation of micropores due to the fact that the in-situ generated metallic K can penetrate into the carbon lattice, and leaving behind the microporosity after removal of the metallic K.^[49,50] As expected, the KOH-activated CTFO (namely CTFC-K-900) exhibited a high SSA value of $2829\text{ m}^2\text{ g}^{-1}$, of which microporosity was above 52% (Table S2, Figure S6).

For the purpose of proving O/N-co-doping, XPS analysis was conducted on CTFC-900 carbon. As shown in Figure 1d, the appearance of C 1s (285.1 eV), N 1s (400.2 eV), and O 1s (532.1 eV) peaks in the full-scan XPS spectrum of CTFC-900 carbon provides direct evidence for O/N-co-doping.^[51,52] Moreover, the deconvoluted N 1s and O 1s peaks indicated that N element has been doped in the configuration of graphitic-N (401.0 eV) and pyridinic-N⁺-O⁻ (403.1 eV),^[51] respectively, whereas O element was doped in the form of C=O (531.3 eV), C-OH/C—O—C (532.5 eV), and COOH (533.8 eV) with the proportions of 31.5%, 41.6% and 26.9% (Figure 1e),^[52] respectively. The elemental composition determined by XPS analysis was found to be 81.92 at% C, 6.98 at% N, and 10.32 at% O for the CTFC-900 carbon (Table S3). Similar to previous studies, the O/N doping level decreased with increasing of the activation temperature.^[34,54] For instance, the N/O contents decreased

from 8.87/13.66 wt% to 7.85/11.47 wt%, and to 4.73/8.21 wt%, respectively, for the CTFC-800, CTFC-900, and CTFC-1000 carbons (Table S1). Notably, the extraordinary high O/N contents together with the extremely high proportion of graphitic-N of CTFC-900 carbon endowed it with not only high wettability, but also high electrical conductivity.^[9,52–54] Contact angle testing provides concrete evidence for the high wettability. As shown in Figure 1f, the CTFC-900 carbon exhibited a small initial contact angle of 51.3° and a fast penetration time of 15 s. In addition, four-probe electrical resistivity testing confirmed that the CTFC-900 carbon had a high electrical conductivity of 670 S m^{-1} .

The morphology and structure of the CTFC-900 carbon were investigated by SEM and TEM analysis. As illustrated in Figure 2a, the CTFC-900 carbon mainly consisted of carbon blocks with irregular shape. The size of such carbon blocks could range from 200 nm to 3 μm . High-magnification SEM image in Figure 2b indicated that the carbon block had a layered structure, which seemed to be very similar to the schist structure (inset of Figure 2b). Such a layered schist structure could be clearly seen in SEM images captured from different sections (Figure 2c, d). With careful observation, the carbon block was actually composed of numerous nanoparticles with the size of several nanometers (inset of Figure 2d). The TEM image in Figure 2e also confirmed the layered structure. High-resolution TEM image captured at the edge of CTFC-900 carbon revealed the partially ordered and porous structure (Figure 2f). The partially graphitic structure was also demonstrated by XRD and Raman analysis (Figure S7a–b), which was also a proof of the high conductivity of CTFC-900 carbon.^[55,56] Elemental mapping images of the CTFC-900 carbon revealed the coexistence of C, N, and O elements that are uniformly distributed (Figure g–j). Additional SEM and TEM images of the CTFC-800 and CTFC-1000 carbons are depicted in Figure S8, demon-

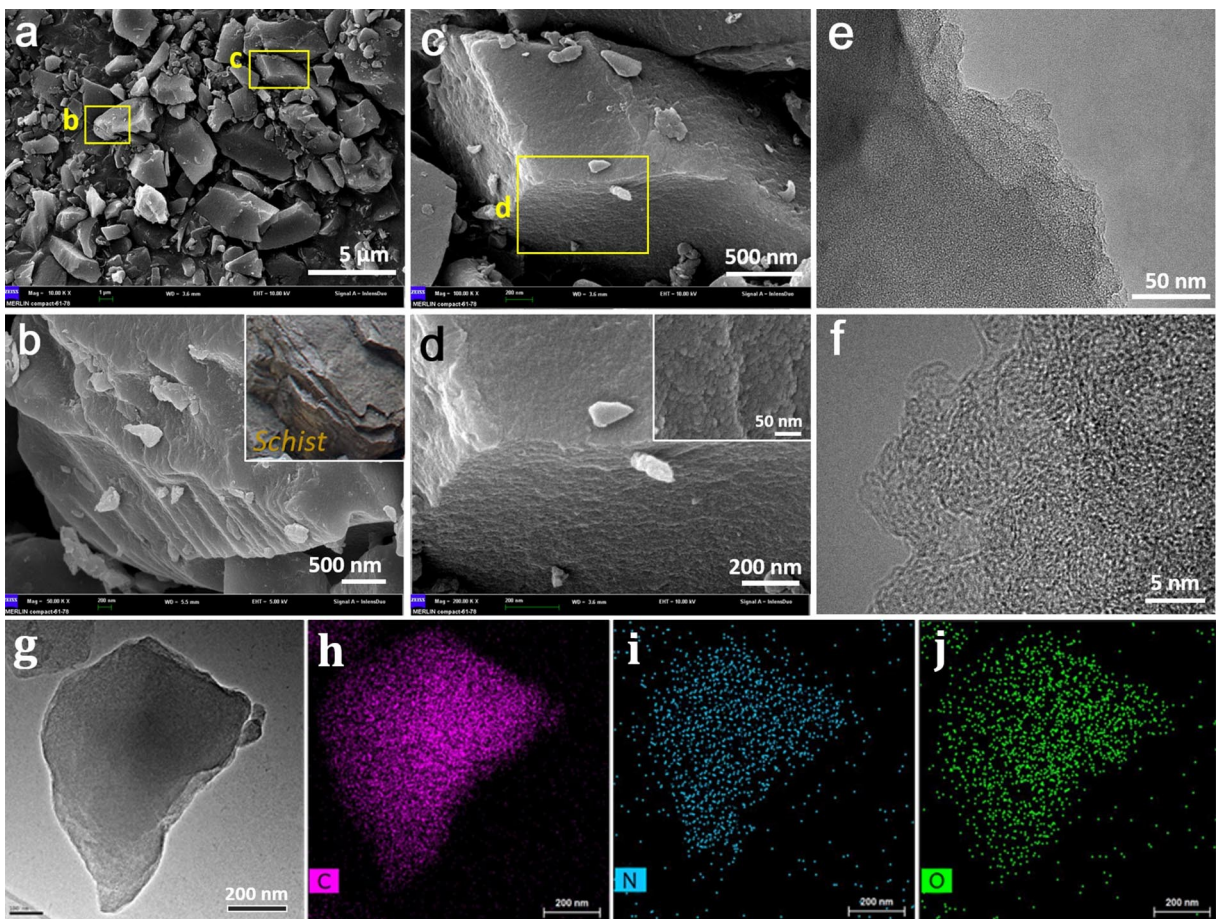


Figure 2. Morphological characterization of CTFC-900. A–d) SEM, e–f) TEM images at different magnifications, and elemental mapping images g–j). Inset: b) optical photograph of schist, and d) high-resolution SEM image.

ing that the activation temperature had almost no impact on the layered structure.

2.2. Supercapacitive Performance of CTFC Carbons

As mentioned above, the layer-structured CTFC carbons have high O/N co-doping level together with high SSA and ultrahigh mesoporosity. Besides, the CTFC carbons also have high conductivity and high wettability, which meet the requirements for the advanced supercapacitors. The supercapacitive behaviors of the symmetric supercapacitors (SCs) that were assembled with these CTFC carbon electrodes in 6.0 M KOH aqueous solution (CTFC-x-SC) were therefore investigated. As shown in Figure 3a, all the CTFC-x-SCs displayed the rectangle-shaped CV profiles at a scanning rate of 0.10 Vs^{-1} . Surprisingly, the rectangular shape could be essentially retained even at an ultrahigh scanning rate of 10 Vs^{-1} except for the CTFC-800-SC (Figure 3b and Figure S9), indicating the ultrahigh-rate capability as well as the ideal EDLC-behavior.^[57,58] The typical GCD curves of these CTFC-x-SCs at 1.0 Ag^{-1} and 100 Ag^{-1} are shown in Figure 3c–d. As can be seen, all the CTFC-x-SCs exhibited a symmetry-shaped GCD profile, suggesting a high electrochemical reversibility.^[59] At a high current loading of 100 Ag^{-1} , the IR

drop was determined to be 197 mV , 58 mV , and 63 mV , respectively, for the CTFC-800-SC, CTFC-900-SC and CTFC-1000-SC, implying the high electrical conductivity and the low ionic resistance.^[57,58] Additional GCD profiles of the CTFC-x-SCs at current loadings that range from 2.0 Ag^{-1} to 1000 Ag^{-1} are shown in Figure S10. As for CTFC-900-SC and CTFC-1000-SC, the linear and symmetrical shape was basically retained at an ultrahigh current loading of 1000 Ag^{-1} . The specific capacitances (C_s) at 1.0 Ag^{-1} are determined to be 287 , 273 , and 254 F g^{-1} , respectively, for the CTFC-900-SC, CTFC-800-SC, and CTFC-1000-SC. In addition, the volume capacitances (C_v) of the CTFC-900-SC, CTFC-800-SC, and CTFC-1000-SC are estimated to be 184 , 160 , and 135 F cm^{-3} , respectively (for details, see the Supporting Information). Notably, the CTFC-900-SC possesses the highest C_s value of 287 F g^{-1} , which is higher than those of recently reported SCs assembled with heteroatom-doped carbon electrodes (Table S4). Such high C_s values for the CTFC-x-SCs should be a balance between EDLC and faradic capacitance. To prove this, kinetic analysis of electrochemical behavior was performed on the CTFC-x-SCs. Figure 3e illustrates the plots of C_s value versus the square root of discharging time (discharge time $^{1/2}$) for CTFC-x-SCs that range from 1.0 to 1000 Ag^{-1} . Typically, the C_s value consists of EDLC that is independent of the discharge time $^{1/2}$ and pseudocapacitance

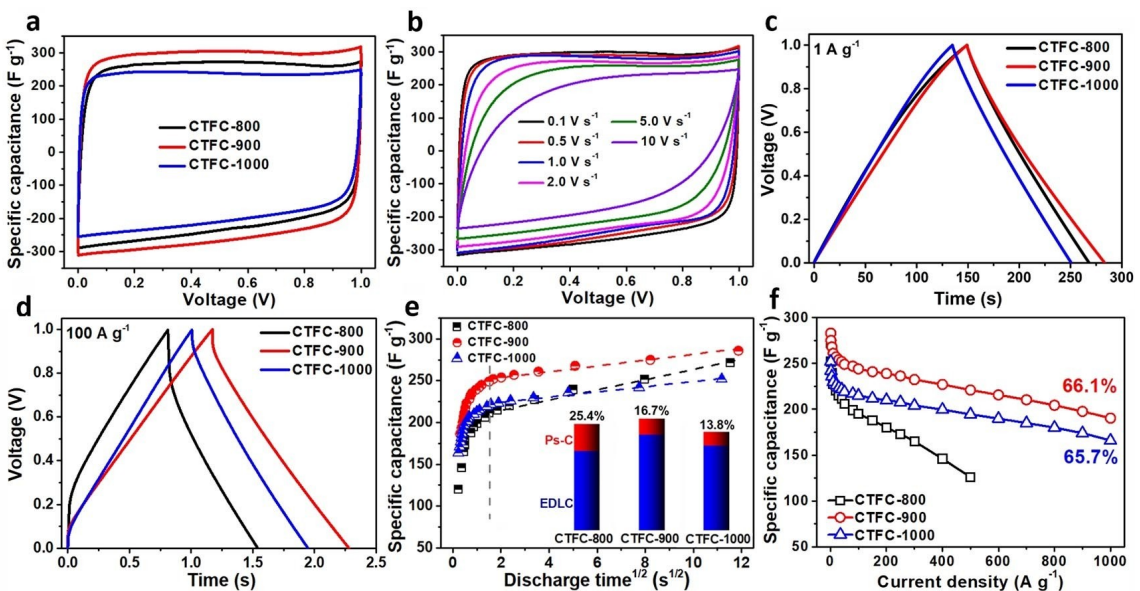


Figure 3. Supercapacitive performance of CTFC-800-SC, CTFC-900-SC, and CTFC-1000-SC in 6.0 M KOH. a) CV curves at a scan rate of 0.10 V s^{-1} . b) CV curves of CTFC-900-SC at different scan rates. c, d) GCD curves at the current densities of 1.0 and 100 A g^{-1} . e) Specific capacitance versus discharge time $^{1/2}$. (Inset: EDLC and Ps-C contributions). f) Specific capacitances versus current densities of 1.0 – 1000 A g^{-1} .

(Ps-C) that is related to the discharge time $^{1/2}$.^[9,60] In the current loading of 1.0 A g^{-1} , the Ps-C contribution for CTFC-800-SC, CTFC-900-SC, and CTFC-1000-SC only accounts for 25.4%, 16.7%, and 13.8%, respectively, of the total C_s value (inset of Figure 3e). This is due to the fact that N-doping in the CTFC carbons is mainly in the form of graphitic-N (~88%), which is conducive to improving the electrical conductivity and therefore to reducing the resistance of electrolyte ion transport during the charge/discharge process.^[52–54] That is to say, the graphitic-N in CTFC carbons plays a very important role in enhancing rate capability, while is only expected to play a minor role in producing faradic capacitance. Among the three CTFC-x-SCs, the CTFC-800 carbon possesses the highest N/O contents (8.87/13.66 wt%) and therefore the highest Ps-C. On the contrary, the CTFC-1000 carbon has the lowest N/O contents (4.73/8.21 wt%) and thus the lowest Ps-C.

The capacitance dependence of the CTFC-x-SCs on the current loadings (1.0 – 1000 A g^{-1}) is shown in Figure 3f. As seen, the capacitances of CTFC-900-SC and CTFC-1000-SC could remain at 189 F g^{-1} and 166 F g^{-1} , respectively, at an ultrahigh current loading of 1000 A g^{-1} . The capacitance retentions of CTFC-900-SC and CTFC-1000-SC at 1.0 – 1000 A g^{-1} can be as high as 66.1% and 65.7%, respectively, demonstrating the ultrahigh-rate capability. On the contrary, the CTFC-800-SC retained a capacitance of 127 F g^{-1} at 500 A g^{-1} , which was around 46.5% of its capacitance at 1.0 A g^{-1} . Notably, such an ultrahigh rate capability of CTFC-900-SC is comparable to many graphene-based SCs and is much higher than those of recently reported SC that derived from heteroatom-doped porous carbons (Table S3). The ultrahigh-rate capability of CTFC-900-SC and CTFC-1000-SC should be attributed to the uniquely layered structure, O/N-co-doping, high SSA, and ultrahigh mesoporosity. As mentioned previously, the CTFC-900 and CTFC-1000

carbons with up to 99% mesoporosity possess high SSA values of $2425 \text{ m}^2 \text{ g}^{-1}$ and $2217 \text{ m}^2 \text{ g}^{-1}$, respectively. The high SSA coupled with ultrahigh mesoporosity in the range of 2.0 – 5.5 nm indicate that the CTFC-900 and CTFC-1000 carbons should have an interconnected mesoporous texture, which not only serves as electrolyte reservoirs, but also allows for fast ion transport.^[34–38] Besides, O/N-co-doping in the CTFC-900 and CTFC-1000 carbons can effectively improve the wettability, hence promoting the pore accessibility for aqueous electrolyte ions. Meanwhile, the remarkably high proportion of graphitic-N in CTFC-900 and CTFC-1000 carbons also plays an important role in enhancing rate capability.^[52–54] Finally, the layered structure of CTFC-900 and CTFC-1000 carbons can simultaneously shorten the distance and decrease the resistance for ion transport, thus ensuring a ultrahigh-rate capability.^[61–63]

The Nyquist plots of the CTFC-x-SCs are shown in Figure 4a. The equivalent series resistance (R_{ESR}) is estimated by extrapolating the vertical portion to the real axis (Figure S11). The R_{ESR} values are determined to be 0.36 ohm , 0.37 ohm , and 0.61 ohm , respectively, for the CTFC-900-SC, CTFC-1000-SC, and CTFC-800-SC. The remarkably small R_{ESR} values for CTFC-900-SC and CTFC-1000-SC provide further evidence for the high electrical conductivity and the low ionic resistance.^[57,58] The Bode plots of CTFC-x-SCs are shown in Figure 4b. As seen, the phase angles are found to be 86.7° , 87.8° , and 88.1° , respectively, for the CTFC-800-SC, CTFC-900-SC and CTFC-1000-SC, again confirming the ideal capacitive behavior.^[64] The time constants (τ_0) are obtained to be 0.12 s , 0.19 s , and 0.52 s , respectively, for the CTFC-900-SC, CTFC-1000-SC, and CTFC-800-SC. The fast response times for the CTFC-900-SC and CTFC-1000-SC are also indicator for the high-rate performance.^[57,58] The Ragone profiles of CTFC-x-SCs are depicted in Figure 4c. As seen, the CTFC-900-SC exhibits a maximum energy density of

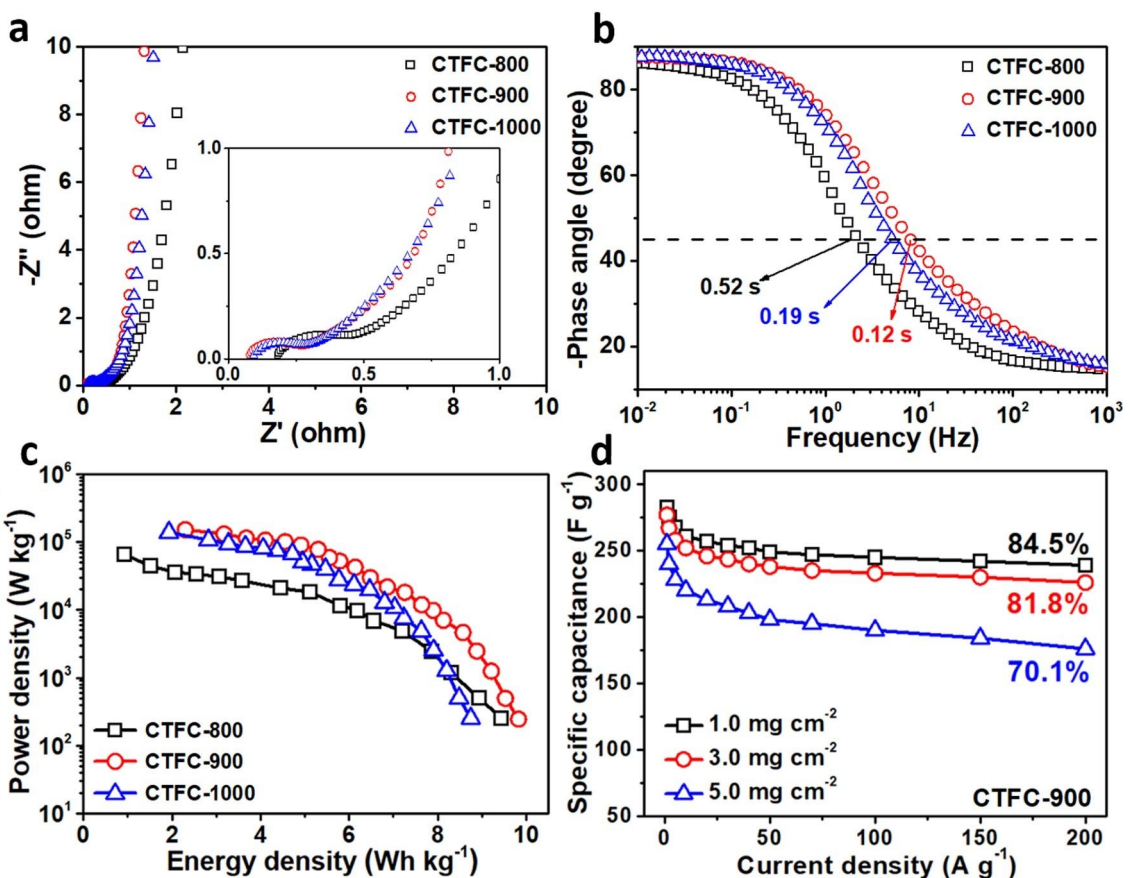


Figure 4. Supercapacitive performance of CTFC-800-SC, CTFC-900-SC, and CTFC-1000-SC in 6.0 M KOH. a) Nyquist plots, b) Bode plots, and c) Ragone plots. d) Capacitances of CTFC-900-SC versus current densities with different mass loadings of 1.0, 3.0, and 5.0 mg cm^{-2} .

9.8 Wh kg^{-1} at a power density of 245.6 W kg^{-1} and the highest power density of 153.1 kW kg^{-1} at 2.3 Wh kg^{-1} .

Considering that the mass loading of active materials in supercapacitors is essential for practical application. The capacitive and high-rate performances of CTFC-900-SC with different CTFC-900 loading (1.0–5.0 mg cm^{-2}) were therefore investigated. As shown in Figure 5e and Figure S12, the C_s value dropped slightly to 256 F g^{-1} as the CTFC-900 loading increased to 5.0 mg cm^{-2} , at least 90.5% of the capacitance at CTFC-900 loading of 1.0 mg cm^{-2} . These results prove that CTFC-900 carbon should have full access to the aqueous KOH electrolyte. Moreover, the CTFC-900-SC can maintain a high level of rate capability with increasing of CTFC-900 loading. For example, the capacitance retentions at 1.0–200 Ag^{-1} are around 84.5%, 81.8%, and 70.1%, respectively, for the CTFC-900 loadings of 1.0 mg cm^{-2} , 3.0 mg cm^{-2} , and 5.0 mg cm^{-2} . These results indicate that CTFC-900 has a great potential for supercapacitor applications.

For the purpose of extending operating voltage, the electrochemical performance of CTFC-900-SC was further examined in 1.0 M Li_2SO_4 neutral electrolyte. The Li_2SO_4 aqueous solution was selected as electrolyte mainly because of its wide operating voltage (~2.2 V) together with the high solubility of Li_2SO_4 in water.^[65,66] In the current case, a stability operating voltage of 2.0 V can be achieved with CTFC-900-SC

as proved by the CV profiles at different potential windows (Figure S13). When the working voltage was set at 2.0 V, the high-rate performance of CTFC-900-SC in neutral electrolyte was again evidenced by a quasi-rectangular CV profile at a high scanning rate of 2.0 Vs^{-1} (Figure 5a) as well as a quasi-triangular GCD profile at a ultrahigh current loading of 500 A g^{-1} (Figure 5b). The capacitance retention at 1–200 Ag^{-1} can be as high as 80.1% for CTFC-900-SC in neutral electrolyte, and still maintains at 64.1% at 1–500 Ag^{-1} (Figure 5c). Such an ultrahigh-rate capability is nearly located in the top level of the carbon-based SCs in neutral electrolyte (Table S4). Moreover, the IR drops are only 0.29 V and 0.62 V, respectively, at the current densities of 200 A g^{-1} and 500 A g^{-1} , which is also an indicator of the low ionic resistance in neutral electrolyte.^[57,58] In addition, a small R_{ESR} (1.8 ohm) and a very fast response time (0.51 s) for CTFC-900-SC in neutral electrolyte were again confirmed by the Nyquist and Bode plots (Figure 5d). The Ragone profiles in Figure 5e indicated that the CTFC-900-SC delivered a high energy density of 32.2 Wh kg^{-1} at a power density of 500 W kg^{-1} . Significantly, the power density reached up to 187.3 kW kg^{-1} at an energy density of 9.1 Wh kg^{-1} , which is far superior to those of carbon-based aqueous SCs and even to some carbon-based organic SCs (Table S3). Such high energy and power densities can enable our device to bridge the energy density gap between commercial electrochemical

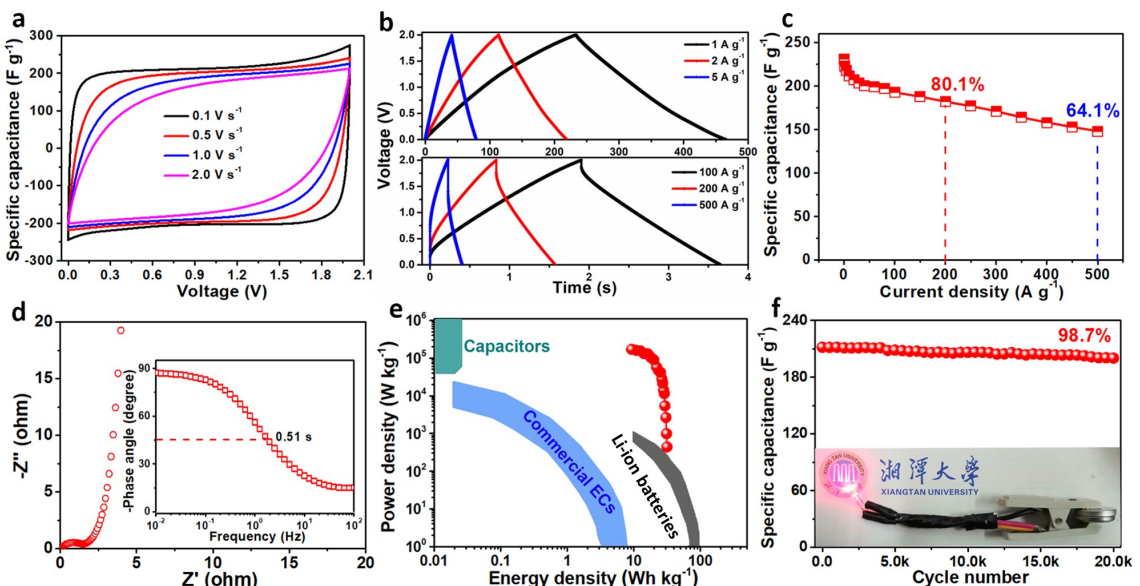


Figure 5. Supercapacitive performance of CTFC-900-SC in 1.0 M Li₂SO₄. a) CV curves at scan rates from 0.1 to 2.0 V s⁻¹. b) GCD curves at current densities from 1.0 to 500 A g⁻¹. c) Specific capacitances versus current densities of 1.0 to 500 A g⁻¹. d) Nyquist and Bode plots. e) Ragone plots (the data for traditional capacitors, commercial ECs, and Li-ion batteries are also presented for comparison). f) Cycling performance (Inset: photograph of a LED powered by CTFC-900-SC).

capacitors (ECs) and Li-ion batteries as well as the power density gap between capacitors and Li-ion batteries (Figure 5e). In addition, The CTFC-900-SC in neutral electrolyte also exhibited excellent cycling stability, retaining 98.7% of its capacitance after 20000 cycles at 10 A g⁻¹ (Figure 5f).

As is noted in the preceding sections, the outstanding supercapacitive performance of our CTFC-900-SC was evidenced by its ultrahigh-rate capability, high energy density, ultrahigh power density, and excellent cycling stability in both alkaline and neutral electrolytes. Such an outstanding performance has been considered to have stemmed from the layered structure, O/N-co-doping, high SSA, and ultrahigh mesoporosity of the CTFC-900 carbon. The CTFC-900 carbon can fully meet the requirements for advanced supercapacitor, i.e., high SSA ($2425 \text{ m}^2 \text{ g}^{-1}$), high porosity with well-defined pore distribution (99% of mesoporosity in the range of 2–5 nm), high electrical conductivity (670 S m^{-1}), and good wettability (with penetration time of 15 s).

3. Conclusions

In summary, O/N-co-doped mesoporous carbons have been successfully fabricated by one-step Na₂CO₃-activation of CTFO precursor. Different from conventionally porous carbons with high SSA but predominant micropores, the as-fabricated O/N-co-doped mesoporous carbon (CTFC-900) had a layered structure, a high pore volume ($1.46 \text{ cm}^3 \text{ g}^{-1}$) together with an ultrahigh mesoporosity (99% in the range of 2–5 nm). Besides, the high N/O contents (6.98 at% N and 10.32 at% O) of CTFC-900 were endowed with not only enhanced wettability but also additional faradaic capacitance. Owing to these merits, the CTFC-900-based supercapacitor exhibited a high specific

capacitance of 287 F g^{-1} at 1.0 A g^{-1} , an ultrahigh rate capability (66.1% of capacitance retention at $1\text{--}1000 \text{ A g}^{-1}$) in alkaline electrolyte. In addition, CTFC-900-SC in neutral electrolyte revealed a high energy density (32.2 Wh kg^{-1}), a ultrahigh power density (187.3 kW kg^{-1}) together with a long cycle-life (98.7% of capacitance retention after 20 000 cycles at 10 A g^{-1}).

Experimental Section

Fabrication of O/N-co-doped mesoporous carbons (CTFC-x)

The experimental details for monomer (2,4,6-tris(4-cyanophenoxy)-1,3,5-triazine) and CTFO syntheses and characterizations have been provided in Supporting Information (Scheme S1–S2, Figure S1–S2). For the fabrication of O/N-co-doped mesoporous carbons, the as-synthesized CTFO was thoroughly blended with Na₂CO₃ at a mass ratio of 1/1 followed by one-step activation at $800\text{--}1000^\circ\text{C}$ for 2 h in N₂, the heating rate of the furnace was 5°C min^{-1} . The O/N-co-doped mesoporous carbons (namely CTFC-x, x indicates the activation temperature, 800, 900, and 1000°C in our case) were obtained after consecutively washing and drying. The carbon yields were around 23.5, 18.7, and 12.3 wt% for CTFC-800, CTFC-900, and CTFC-1000, respectively.

Electrochemical measurements

The fabrication processes for symmetric supercapacitors are shown in Supporting Information. All electrochemical measurements were done on a Gamry-1010E electrochemical workstation. Cyclic voltammetry (CV), galvanostatic charging and discharging (GCD), and electrochemical impedance spectroscopy (EIS) were used to estimate the CTFC carbon-based supercapacitors.

Acknowledgements

Financial support from program for NSFC (51674219) and the Construct Program of the Key Discipline in Hunan Province is greatly acknowledged.

Conflict of Interest

The authors declare no conflict of interest.

Keywords: O/N co-doping • layered structure • mesoporous carbon • ultrahigh-rate • supercapacitors

- [1] M. Salanne, B. Rotenberg, K. Naoi, K. Kaneko, P.-L. Taberna, C. P. Grey, B. Dunn, P. Simon, *Nat. Energy* **2016**, *1*, 1–10.
- [2] Q. Zhu, D. Zhao, M. Cheng, J. Zhou, K. A. Owusu, L. Mai, Y. Yu, *Adv. Energy Mater.* **2019**, *9*, 1901081.
- [3] S. Zhang, N. Pan, *Adv. Energy Mater.* **2015**, *5*, 1401401.
- [4] F. Béguin, V. Presser, A. Balducci, E. Frackowiak, *Adv. Mater.* **2014**, *26*, 2219–2251.
- [5] T. Chen, L. Dai, *Mater. Today* **2013**, *16*, 272–280.
- [6] L. L. Zhang, X. S. Zhao, *Chem. Soc. Rev.* **2009**, *38*, 2520–2531.
- [7] Y. Jiao, P. Jian, Y. Chunshuang, C. Dahong, H. Yongyuan, C. Gang, *J. Mater. Chem. A* **2016**, *4*, 13344–13351.
- [8] W. Zuo, R. Li, C. Zhou, Y. Li, J. Xia, J. Liu, *Adv. Sci.* **2017**, *4*, 1600539.
- [9] T. Lin, I.-W. Chen, F. Liu, C. Yang, H. Bi, F. Xu, F. Huang, *Science* **2015**, *350*, 1508–1513.
- [10] H. Wang, Z. Yu, M. F. El-Kady, M. Anderson, M. D. Kowal, M. Li, R. B. Kaner, *Energy Storage Mater.* **2019**, *19*, 137–147.
- [11] M. S. Javed, S. S. A. Shah, S. Hussain, S. Tan, W. Mai, *Chem. Eng. J.* **2020**, *382*, 122814.
- [12] W. Jiang, D. Yu, Q. Zhang, K. Goh, L. Wei, Y. Yong, R. Jiang, J. Wei, Y. Chen, *Adv. Funct. Mater.* **2015**, *25*, 1063–1073.
- [13] G. Wang, L. Zhang, J. Zhang, *Chem. Soc. Rev.* **2012**, *41*, 797–828.
- [14] B. Liu, Y. Liu, H. Chen, M. Yang, H. Li, *ACS Sustainable Chem. Eng.* **2019**, *7*, 3101–3110.
- [15] P. Giannakou, M. G. Masteghin, R. C. T. Slade, S. J. Hinder, M. Shkunov, *J. Mater. Chem. A* **2019**, *7*, 21496–21506.
- [16] X. Gao, P. Wang, Z. Pan, J. P. Claverie, J. Wang, *ChemSusChem* **2020**, *13*, 1226–1254.
- [17] S. Sanati, Z. Rezvani, *Chem. Eng. J.* **2019**, *362*, 743–757.
- [18] C. Zhu, P. Yang, D. Chao, X. Wang, X. Zhang, S. Chen, B. K. Tay, H. Huang, H. Zhang, W. Mai, H. J. Fan, *Adv. Mater.* **2015**, *27*, 4566–4571.
- [19] K. Wang, H. Wu, Y. Meng, Z. Wei, *Small* **2014**, *10*, 14–31.
- [20] Y. Wang, F. Chen, Z. Liu, Z. Tang, Q. Yang, P. Y. Zhao, P. S. Du, P. Q. Chen, P. C. Zhi, *Angew. Chem. Int. Ed.* **2019**, *58*, 15707–15711.
- [21] H. Wang, Z. Yu, M. F. El-Kady, M. Anderson, M. D. Kowal, M. Li, R. B. Kaner, *Energy Storage Mater.* **2019**, *19*, 137–147.
- [22] J. Yang, H. Wu, M. Zhu, W. Ren, Y. Lin, H. Chen, F. Pan, *Nano Energy* **2017**, *33*, 453–461.
- [23] P. Simon, Y. Gogotsi, *Nat. Mater.* **2008**, *7*, 845.
- [24] M. Liu, J. Qian, Y. Zhao, D. Zhu, L. Gan, L. Chen, *J. Mater. Chem. A* **2015**, *3*, 11517–11526.
- [25] H. Wang, Z. Xu, A. Kohandehghan, Z. Li, K. Cui, X. Tan, T. J. Stephenson, C. K. King'ondu, C. M. B. Holt, B. C. Olsen, J. K. Tak, D. Harfield, A. O. Anyia, D. Mitlin, *ACS Nano* **2013**, *7*, 5131–5141.
- [26] D. Kang, Q. Liu, J. Gu, Y. Su, W. Zhang, D. Zhang, *ACS Nano* **2015**, *9*, 11225–11233.
- [27] Z. Song, H. Duan, D. Zhu, Y. Lv, W. Xiong, T. Cao, L. Li, M. Liu, L. Gan, *J. Mater. Chem. A* **2019**, *7*, 15801–15811.
- [28] D. Xue, D. Zhu, H. Duan, Z. Wang, Y. Lv, W. Xiong, L. Li, M. Liu, L. Gan, *Chem. Commun.* **2019**, *55*, 11219–11222.
- [29] Z. Song, L. Miao, L. Li, D. Zhu, Y. Lv, W. Xiong, H. Duan, Z. Wang, L. Gan, M. Liu, *J. Mater. Chem. A* **2020**, *8*, 3717–3725.
- [30] L. Miao, H. Duan, Z. Wang, Y. Lv, W. Xiong, D. Zhu, L. Gan, L. Li, M. Liu, *Chem. Eng. J.* **2020**, *382*, 122945.
- [31] J. Niu, R. Shao, J. Liang, M. Dou, Z. Li, Y. Huang, F. Wang, *Nano Energy* **2017**, *36*, 322–330.
- [32] R. Ryoo, S. H. Joo, M. Kruk, M. Jaroniec, *Adv. Mater.* **2001**, *13*, 677–681.
- [33] Y. Korenblit, M. Rose, E. Kockrick, L. Borchardt, A. Kvist, S. Kaskel, G. Yushin, *ACS Nano* **2010**, *4*, 1337–1344.
- [34] X. Wei, X. Jiang, J. Wei, S. Gao, *Chem. Mater.* **2016**, *28*, 445–458.
- [35] L. Qie, W. Chen, H. Xu, X. Xiong, Y. Jiang, F. Zou, X. Hu, Y. Xin, Z. Zhang, Y. Huang, *Energy Environ. Sci.* **2013**, *6*, 871–878.
- [36] T. Y. Wei, C. H. Chen, H. C. Chien, S. Y. Lu, C. C. Hu, *Adv. Mater.* **2010**, *22*, 347–351.
- [37] J. W. Lee, T. Ahn, J. H. Kim, J. M. Ko, J. D. Kim, *Electrochim. Acta* **2011**, *56*, 4849–4857.
- [38] L. Wang, X. Liu, X. Wang, X. Yang, L. Lu, *Curr. Appl. Phys.* **2010**, *10*, 1422–1426.
- [39] J. Chmiola, G. Yushin, Y. Gogotsi, C. Portet, P. Simon, P. L. Taberna, *Science* **2006**, *313*, 1760–1763.
- [40] Q. Wang, J. Yan, Z. Fan, *Energy Environ. Sci.* **2016**, *9*, 729–762.
- [41] Y. Mao, H. Duan, B. Xu, L. Zhang, Y. Hu, C. Zhao, Z. Wang, L. Chen, Y. Yang, *Energy Environ. Sci.* **2012**, *5*, 7950–7955.
- [42] L.-L. Zhang, H.-H. Li, Y.-H. Shi, C.-Y. Fan, X.-L. Wu, H.-F. Wang, H.-Z. Sun, J.-P. Zhang, *ACS Appl. Mater. Interfaces* **2016**, *8*, 4233–4241.
- [43] L. Jiao, Y. Hu, H. Ju, C. Wang, M.-R. Gao, Q. Yang, J. Zhu, S.-H. Yu, H.-L. Jiang, *J. Mater. Chem. A* **2017**, *5*, 23170–23178.
- [44] D. Baumann, C. Lee, C. Wan, H. Sun, X. Duan, *ACS Mater. Lett.* **2019**, *1*, 320–326.
- [45] M. M. Vadiyar, X. Liu, Z. Ye, *ACS Appl. Mater. Interfaces* **2019**, *11*, 45805–45817.
- [46] D.-G. Wang, H. Wang, Y. Lin, G. Yu, M. Song, W. Zhong, G.-C. Kuang, *ChemSusChem* **2018**, *11*, 3932–3940.
- [47] K. Y. Foo, B. H. Hameed, *Chem. Eng. J.* **2012**, *184*, 57–65.
- [48] D. Guo, S. Wu, B. Liu, X. Yin, Q. Yang, *Appl. Energy* **2012**, *95*, 22–30.
- [49] J. Romanos, M. Beckner, T. Rash, L. Firlej, B. Kuchta, P. Yu, G. Suppes, C. Wexler, P. Pfeifer, *Nanotechnology* **2012**, *23*, 015401.
- [50] R. L. Zornetta, K. M. Barcelos, F. G. E. Nogueira, L. A. M. Ruotolo, *Carbon* **2020**, *156*, 346–358.
- [51] L. Qie, W. Chen, H. Xu, X. Xiong, Y. Jiang, F. Zou, X. Hu, Y. Xin, Z. Zhang, Y. Huang, *Energy Environ. Sci.* **2013**, *6*, 2497–2504.
- [52] T. Kim, Y. H. Mo, K. S. Nahm, S. M. Oh, *J. Power Sources* **2006**, *162*, 1275–1281.
- [53] S. C. Hou, X. Cai, H. W. Wu, X. Yu, M. Peng, K. Yan, D. C. Zou, *Energy Environ. Sci.* **2013**, *6*, 3356–3362.
- [54] W. Shen, C. Wang, Q. Xu, H. Liu, Y. Wang, *Adv. Energy Mater.* **2015**, *5*, 1400982.
- [55] M. Sevilla, A. B. Fuertes, *ACS Nano* **2014**, *8*, 5069–5078.
- [56] J. Liang, Y. Jiao, M. Jaroniec, S. Z. Qiao, *Angew. Chem. Int. Ed.* **2012**, *51*, 11496–11500; *Angew. Chem.* **2012**, *124*, 11664–11668.
- [57] Y. Bu, T. Sun, Y. Cai, L. Du, O. Zhuo, L. Yang, Q. Wu, X. Wang, Z. Hu, *Adv. Mater.* **2017**, *29*, 700470.
- [58] J. Zhao, Y. Jiang, H. Fan, M. Liu, O. Zhuo, X. Wang, Q. Wu, L. Yang, Y. Ma, Z. Hu, *Adv. Mater.* **2017**, *29*, 1604569.
- [59] K. Xie, X. Qin, X. Wang, Y. Wang, H. Tao, Q. Wu, L. Yang, Z. Hu, *Adv. Mater.* **2012**, *24*, 347–352.
- [60] V. Augustyn, J. Come, M. A. Lowe, J. W. Kim, P.-L. Taberna, S. H. Tolbert, H. D. Abruna, P. Simon, B. Dunn, *Nat. Mater.* **2013**, *12*, 518–522.
- [61] Y. Dong, M. Yu, Z. Wang, Y. Liu, X. Wang, Z. Zhao, J. Qiu, *Adv. Funct. Mater.* **2016**, *26*, 7590–7598.
- [62] H. Wang, L. Zhi, K. Liu, L. Dang, Z. Liu, Z. Lei, C. Yu, J. Qiu, *Adv. Funct. Mater.* **2015**, *25*, 5420–5427.
- [63] X. Fan, C. Yu, J. Yang, Z. Ling, C. Hu, M. Zhang, J. Qiu, *Adv. Energy Mater.* **2015**, *5*, 1401761.
- [64] J. Zhao, H. Lai, Z. Lyu, Y. Jiang, K. Xie, X. Wang, Q. Wu, L. Yang, Z. Jin, Y. Ma, J. Liu, Z. Hu, *Adv. Mater.* **2015**, *27*, 3541–3545.
- [65] Q. Gao, L. Demarconnay, E. Raymundo-Piñero, F. Béguin, *Energy Environ. Sci.* **2012**, *5*, 9611.
- [66] L. Wang, G. Zhang, B. Han, Y. Chang, H. Li, J. Wang, C. Hu, Z. Chang, Z. Huo, X. Sun, *J. Mater. Chem. A* **2017**, *5*, 6734–6739.

Manuscript received: February 20, 2020
Revised manuscript received: May 25, 2020
Accepted manuscript online: June 8, 2020
Version of record online: July 2, 2020